

Non-Equilibrium Edge Channel Spectroscopy in the Integer Quantum Hall Regime

C. Altimiras,¹ H. le Sueur,¹ U. Gennser,¹ A. Cavanna,¹ D. Maily,¹ and F. Pierre^{1,*}

¹CNRS, Laboratoire de Photonique et de Nanostructures (LPN) - Phynano team, route de Nozay, 91460 Marcoussis, France

(Dated: October 14, 2009)

Heat transport has large potentialities to unveil new physics in mesoscopic systems. A striking illustration is the integer quantum Hall regime¹, where the robustness of Hall currents limits information accessible from charge transport². Consequently, the gapless edge excitations are incompletely understood. The effective edge states theory describes them as prototypical one-dimensional chiral fermions^{3,4} - a simple picture that explains a large body of observations⁵ and calls for quantum information experiments with quantum point contacts in the role of beam splitters^{6,7,8,9,10,11}. However, it is in ostensible disagreement with the prevailing theoretical framework that predicts, in most situations¹², additional gapless edge modes¹³. Here, we present a setup which gives access to the energy distribution, and consequently to the energy current, in an edge channel brought out-of-equilibrium. This provides a stringent test of whether the additional states capture part of the injected energy. Our results show it is not the case and thereby demonstrate regarding energy transport, the quantum optics analogy of quantum point contacts and beam splitters. Beyond the quantum Hall regime, this novel spectroscopy technique opens a new window for heat transport and out-of-equilibrium experiments.

The integer quantum Hall effect, discovered nearly thirty years ago¹, has recently experienced a strong revival driven by milestone experiments toward quantum information with edge states^{8,9,14}. Beyond Hall currents, new phenomena have emerged that were unexpected within the free one-dimensional chiral fermions (1DCF) model. The on-going debate triggered by electronic Mach-Zehnder interferometers experiments^{8,15,16,17} vividly illustrates the gaps in our understanding. Coulomb interaction is seen as the key ingredient. In addition to its most striking repercussion, the fractional quantum Hall effect¹⁸, the edge reconstruction (ER) turns out to have deep implications on edge excitations. This phenomenon results from the competition between Coulomb interaction that tends to spread the electronic fluid, and the confinement potential: as the latter gets smoother, the non-interacting edge becomes unstable¹⁹. Theory predicts new branches of gapless electronic excitations in reconstructed edges^{13,20}, which breaks the mapping of an edge channel (EC) onto 1DCF and, possibly, the promising quantum optics analogy. For most edges realized in semi-conductor heterojunctions (except by cleaved edge overgrowth²¹), ER results in wide compressible ECs separated by narrow incompressible strips¹² and the new excited states are overall neutral internal charge oscillations across the ECs width¹³.

In practice, the predicted additional neutral modes are

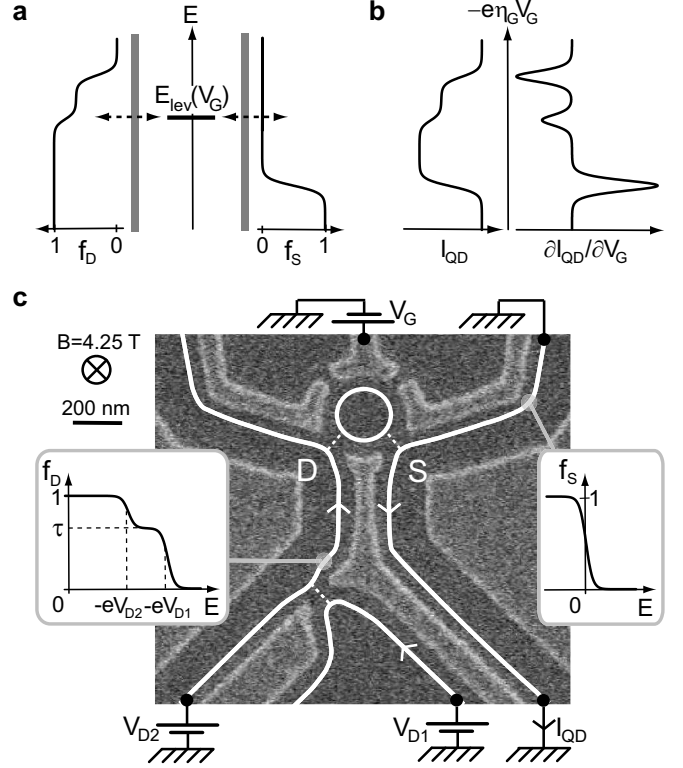


Figure 1: **Experimental implementation of non-equilibrium edge channel spectroscopy.** **a**, Schematic description of the energy distributions $f_{D,S}(E)$ spectroscopy with a single active electronic level of tunable energy $E_{lev}(V_G)$ in the quantum dot (QD). **b**, The current I_{QD} ($\partial I_{QD}/\partial V_G$) is proportional to $f_S(E) - f_D(E)$ ($\partial(f_S(E) - f_D(E))/\partial E$) ignoring variations in tunnel rates and tunneling density of states. **c**, E-beam micrograph of the sample. Surface metal gates appear brighter. Electronic excitations propagate counter clockwise along two edge channels (EC) of the quantum Hall regime. The outer EC (continuous white lines) is partly transmitted (dashed lines) across quantum point contact (QPC) and QD. The inner EC (not shown) is always reflected. The QPC is used to drive out-of-equilibrium the drain outer EC. Gates partly covered by the insets are grounded and do not influence the electron paths. Left inset: non-interacting electrons prediction for $f_D(E)$ in the outer EC at output of QPC.

transparent to Hall currents. More surprisingly, a linear I-V characteristic is frequently observed for tunnel contacts (different behaviors were also reported, e.g.²²) whereas a non-linear characteristic is predicted^{23,24,25}. This contradiction is resolved by assuming *ad-hoc* that only *rigid displacements* of compressible ECs are excited by tunnel events, and not internal excitations^{13,23,24,26}.

The rigid displacement model arguably relies on the overriding strength of Coulomb interaction that tends to orthogonalize bare tunneling electrons and correlated electronic fluids²⁶. However, the above argument does not hold at arbitrary transmission probabilities, where multiple electrons processes occur. Therefore, the role of predicted internal excitations has to be determined experimentally. The present work provides such a test. An EC is driven out-of-equilibrium with a quantum point contact (QPC) of arbitrary transmission, possibly exciting internal modes. A short distance away, the resulting energy distribution $f(E)$ is measured with a tunnel coupled quantum dot (QD) expected to probe only rigid displacement excitations, hereafter called quasiparticles. Consequently, the amount of energy injected into internal modes at the QPC would appear as an energy loss in $f(E)$.

Measurements of the energy distribution in mesoscopic devices were first performed in 1997 on metallic circuits using a superconducting tunnel probe²⁷. More recently, the regime of high magnetic fields was accessed using dynamical Coulomb blockade²⁸. In two-dimensional electron gas systems, non-Fermi energy distributions could not be measured since transferring the techniques developed for metal circuits is technically challenging (although hot electrons have been detected, e.g.²⁹). Regarding the quantum Hall regime (QHR), state of the art is the very recent qualitative probe of heating³⁰. Here, we demonstrate that $f(E)$ can be fully extracted from the tunnel current across a QD. In the sequential tunneling regime, the discrete electronic levels in a QD behave as energy filters^{31,32}, as previously demonstrated with double QDs³³. Assuming a single active QD level of energy E_{lev} , and ignoring the energy dependence of tunnel rates and tunneling density of states in the electrodes, the QD current reads

$$I_{\text{QD}} = I_{\text{QD}}^{\text{max}} (f_S(E_{lev}) - f_D(E_{lev})), \quad (1)$$

where the subscript S (D) refers to the source (drain) electrode; $f_{S,D}$ are the corresponding energy distributions and $I_{\text{QD}}^{\text{max}}$ is the maximum QD current. In practice, $f_{S,D}$ are obtained separately by applying a large enough source-drain voltage (Fig. 1a,b) and the probed energy $E_{lev} = E_0 - e\eta_G V_G$ is swept using a capacitively coupled gate biased at V_G , with η_G the gate voltage-to-energy lever arm and E_0 an offset. Raw data $\partial I_{\text{QD}}/\partial V_G$ measured by lock-in techniques are proportional to $\partial f_{D,S}(E)/\partial E$.

A tunable non-Fermi energy distribution is generated in an EC with a voltage biased QPC. Similar setups were used previously to create imbalanced electron populations between co-propagating ECs³⁴, each characterized by a cold Fermi distribution. Only in a very recent experiment³⁰, was an EC heated up. Beyond heating, $f(E)$ is here controllably tuned out of equilibrium. Let us consider one EC and assume it can be mapped onto non-interacting 1DCF. According to the scattering approach³⁵, the energy distribution at the output of a

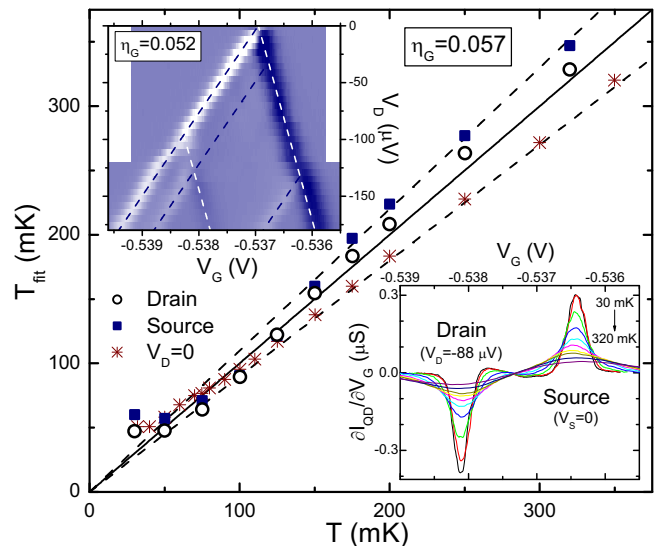


Figure 2: Equilibrium edge channel spectroscopy and quantum dot characterization. Temperatures T_{fit} are obtained by fitting the QD-drain dip (\circ) and QD-source peak (\blacksquare) in $\partial I_{\text{QD}}/\partial V_G$ (resp. left and right peaks in bottom right inset), and from the single $\partial I_{\text{QD}}/\partial V_D$ peak at $V_D = 0$ ($*$) (raw data not shown) with $\eta_G = 0.057$. We assumed a single active level in the QD and Fermi energy distributions in source and drain. Errors within $T \pm 10\%$ are enclosed between the dashed lines. Top left inset: Surface plot of $\partial I_{\text{QD}}/\partial V_G$ (negative is brighter, positive darker) measured at $T = 30$ mK for an outer (inner) drain EC biased at V_D (-88 μV). The intense stripes slopes yield $\eta_G = 0.052 \pm 9\%$. Enclosed dashed lines outline the small contributions of other electronic levels.

QPC of transmission τ is a tunable double step (Fig. 1c, left inset)

$$f_D(E) = \tau f_{D1}(E) + (1 - \tau) f_{D2}(E), \quad (2)$$

where f_{D1} (f_{D2}) is the equilibrium Fermi distribution function in the partially transmitted (reflected) incoming EC of electrochemical potential shifted by eV_{D1} (eV_{D2}). In presence of ER, the above energy distribution applies to the quasiparticles if internal modes are not excited at the QPC. Else, there are no theoretical predictions because a QPC is very difficult to treat non-perturbatively in their natural bosonic formalism.

The sample shown in Fig. 1c was tailored in a two-dimensional electron gas realized in a GaAs/Ga(Al)As heterojunction, set to filling factor 2 and measured in a dilution refrigerator of base temperature 30 mK. The experiment detailed here focuses on the outer EC represented as a white line. The inner EC (not shown) is fully reflected by the QPC and the QD. We checked that charge tunneling between ECs is negligible along the 0.8 μm propagation length from QPC to QD.

We first perform a standard non-linear QD characterization³² (Fig. 2, top left inset). The two large signal stripes are frontiers of consecutive Coulomb diamonds and are accounted for by a single active QD

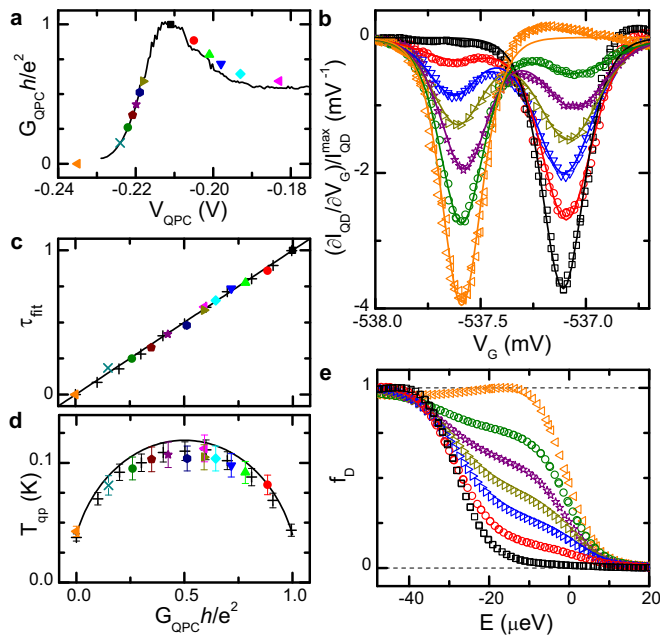


Figure 3: **Spectroscopy of an edge channel tuned out-of-equilibrium with the conductance of a QPC.** The QPC's voltage bias is here fixed to $\delta V_D \equiv V_{D1} - V_{D2} = 36 \mu\text{V}$. Data shown as (+) in (c) and (d) were obtained in a second cooldown with a renewed $\eta_G = 0.059 \pm 7\%$. **a**, Measured G_{QPC} versus V_{QPC} applied to the lower left metal gate in Fig. 1c. Symbols are data points obtained during the corresponding EC spectroscopy. The continuous line was measured earlier with $\delta V_D = 0$. **b**, Measured $\partial I_{\text{QD}}/\partial V_G$ (symbols) for the QD-drain contribution (data have been aligned in V_G and normalized to $I_{\text{QD}}^{\text{max}}$). The two dips correspond to a double step energy distribution $f_D(E)$. **c**, Symbols are τ_{fit} obtained from fits of the data (continuous lines in (b)) assuming $f_D(E)$ is the weighted sum of two Fermi functions. We find an accurate agreement with the non-interacting 1D chiral fermions (1DCF) model prediction $\tau_{\text{fit}} = G_{\text{QPC}}h/e^2$. **d**, Generalized non-equilibrium temperature (symbols, see text) extracted from the data and theoretical prediction for free 1DCF (continuous line). Error bars are dominated by uncertainties on η_G . **e**, Energy distributions obtained by integrating the data in (b).

level. Small contributions of three additional levels of relative energies $\{-95, 30, 130\} \mu\text{eV}$ are also visible. The lever arm extracted from the stripes' slopes is $\eta_G \simeq 0.052 \pm 9\%$.

Then, we test the spectroscopy with known Fermi functions by measuring $\partial I_{\text{QD}}/\partial V_G(V_G)$ at $V_{D1} = V_{D2} = -88 \mu\text{V}$ for several temperatures (Fig. 2, bottom right inset). By fitting these data with Eq. 1 using Fermi functions, we extract a fit temperature scaled by the lever arm T_{fit}/η_G . The value $\eta_G = 0.057$, compatible with the non-linear QD characterization, is found to reproduce best the mixing chamber temperature T with T_{fit} . The drain (o) and source (■) fit temperatures are shown in Fig. 2 together with T_{fit} obtained using the standard procedure³² from $\partial I_{\text{QD}}/\partial V_D(V_G)$ at $V_D \simeq 0$ (*). We find

deviations mostly within $\pm 10\%$ (dashed lines in Fig. 2) except for a saturation at $T_{\text{fit}} \approx 50 \text{ mK}$ possibly due to a higher electronic temperature. In the following, we use $\eta_G = 0.057$ obtained here in the same experimental configuration as to measure unknown $f(E)$ s.

Electrons are now driven out-of-equilibrium in the drain outer EC. In the following, the electrode $D2$ and the inner drain EC are voltage biased at $V_{D2} = -88 \mu\text{V}$ and the source ECs are emitted by a cold ground.

First, the bias voltage across the QPC is set to $\delta V_D \equiv V_{D1} - V_{D2} = 36 \mu\text{V}$ and its conductance $G_{\text{QPC}} = \tau e^2/h$ is tuned by applying V_{QPC} to the bottom left gate in Fig. 1c (see Fig. 3a). Note that at 30 mK, we find the transmission τ is constant within 2% with the QPC voltage bias below $36 \mu\text{V}$. Typical sweeps $\partial I_{\text{QD}}/\partial V_G(V_G)$ and the corresponding $f_D(E)$ are shown in Figs. 3b and 3e, respectively. The QD-drain negative contribution transforms from a single dip at $\tau = \{0, 1\}$ into two dips separated by a fixed gate voltage and whose relative weights evolve monotonously with $\tau \in]0, 1[$. Continuous lines are fits with Eq. 2 using for $f_{D1, D2}$ two Fermi functions shifted by a fixed energy and weighted by the factors τ_{fit} and $1 - \tau_{\text{fit}}$. The values of τ_{fit} are found to deviate by less than 0.03 from the measured transmission τ (Fig. 3c), in accurate agreement with the free 1DCF model. Symbols (+) in Fig. 3 correspond to data obtained in a second cooldown.

In a second step, the QPC transmission is fixed to $\tau \approx 0.5$ and the bias voltage δV_D is changed. Typical raw data are shown in Fig. 4a. These were obtained in a third cooldown with a QD renewed by the thermal cycle showing no signs of additional QD levels in the probed energy range. The single dip in the QD-drain contribution (bright) at $\delta V_D = 0$ splits in two similar dips that are separated by a gate voltage difference proportional to δV_D . Meanwhile, the QD-source peak (dark) is mostly unchanged but slowly drifts parallel to one QD-drain dip due to the capacitive coupling between drain and QD. In the first cooldown, V_{D1} was kept within $[-106, -34] \mu\text{V}$ to minimize complications related to additional QD levels (lower bound) and to ensure well-separated source and drain contributions (upper bound). Symbols in Figs. 4b and 4e are, respectively, data and extracted $f_D(E)$ for the QD-drain contribution at $\delta V_D = \{-18, 0, 18, 27, 36, 45, 54\} \mu\text{V}$ and $\tau = 0.58$. Continuous lines in Fig. 4b are fits with Eq. 2 using the measured τ and for $f_{D1, D2}$ two Fermi functions shifted in energy by the fit parameter $-e\eta_G\delta V_G$. The resulting $\eta_G\delta V_G$ are plotted as symbols versus δV_D in Fig. 4c. Those obtained in the third cooldown are shown as (*) using the renewed lever arm $\eta_G = 0.062$. We find $\eta_G\delta V_G \simeq \delta V_D$ as expected from the non-interacting 1DCF model. Deviations are always smaller than $8 \mu\text{V}$ ($5 \mu\text{V}$) for the first (third) cooldown, a reasonable agreement regarding uncertainties in η_G of $\pm 10\%$ ($\pm 5\%$).

In the two experiments above, we found the measured quasiparticle $f(E)$ s verify predictions of the scattering approach. In order to establish the analogy QPC-beam

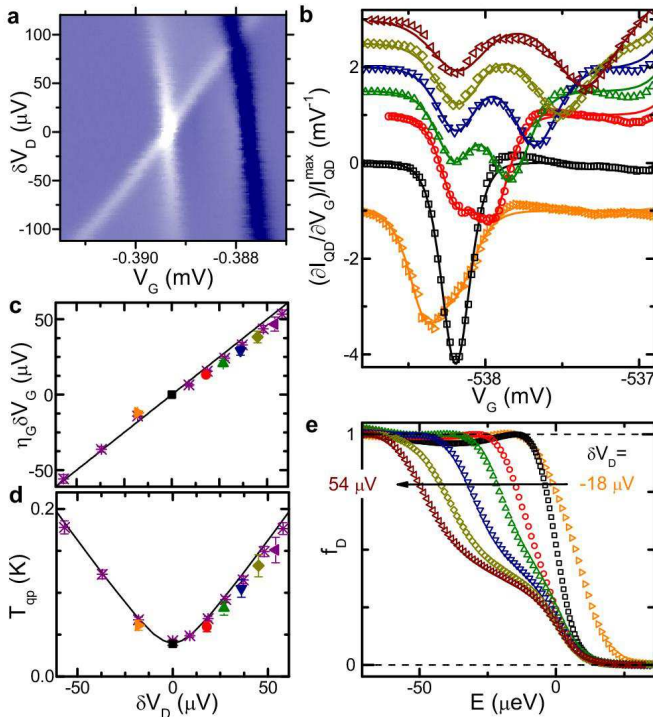


Figure 4: **Spectroscopy of an edge channel tuned out-of-equilibrium with the voltage across a QPC.** The QPC's conductance is here fixed to $G_{\text{QPC}} \approx 0.5e^2/h$. Data of (a) and (*) in (c) and (d) were obtained in a third cooldown with a renewed $\eta_G = 0.062 \pm 5\%$. **a**, Surface plot of $\partial I_{\text{QD}}/\partial V_G(\delta V_D, V_G)$. The QD-drain contribution (brighter) splits into two similar dips separated by a gate voltage difference proportional to δV_D . **b**, Measured $\partial I_{\text{QD}}/\partial V_G$ (symbols) for the QD-drain contribution. Data have been shifted vertically for clarity, and horizontally to align the peak corresponding to the fixed potential V_{D2} . Continuous lines are fits assuming $f_D(E)$ is the weighted sum of two Fermi functions. **c**, Symbols are the fit parameters $\eta_G \delta V_G$. The continuous line is the prediction for non-interacting 1DCF. **d**, Generalized non-equilibrium temperature (symbols) and theoretical prediction for free 1DCF (continuous line). The good agreement data-prediction demonstrates that internal modes are not excited at the QPC within our experimental accuracy. **e**, Energy distributions obtained by integrating the data in (b).

splitter one also needs to demonstrate that internal EC modes are not excited. A direct test consists in extracting the quasiparticle heat current J_E^{qp} from the data, and comparing it with the full edge excitations heat current J_E obtained from power balance considerations (see Supplementary Information for details):

$$J_E(T=0) = \frac{(e\delta V_D)^2}{2h} \tau(1-\tau). \quad (3)$$

The cancellation $v\nu = 1/h$ of velocity (v) and density of states per unit length and energy (ν) that applies to the 1DCF quasiparticles permits us to obtain J_E^{qp} from the measured $f(E)$ without any sample specific parameters:

$$J_E^{qp} = \frac{1}{h} \int (E - \mu)(f(E) - \theta(\mu - E))dE, \quad (4)$$

with μ the electrochemical potential and $\theta(E)$ the step function. Consequently, *we measure quantitatively the quasiparticle heat current*. The result of this procedure is shown as symbols in Figs. 3d and 4d using the generalized non-equilibrium temperature $T_{qp} \equiv \sqrt{6hJ_E^{qp}/\pi k_B}$ together with the prediction $T_{1DCF} = \sqrt{T^2 + \tau(1-\tau)3(e\delta V_D/\pi k_B)^2}$ if none of the injected power is carried on by internal modes (continuous lines). We find a good agreement $T_{qp} \simeq T_{1DCF}$ without fitting parameters and essentially in or close to error bars. Hence, within our experimental accuracy, the propagative internal modes do not contribute to heat transport and therefore are not excited. Note that the relatively small observed deviations are cooldown dependent, which points out the QD. Indeed, the data can be more accurately accounted for including a second active QD level (see Supplementary Information). Last, preliminary data show a significant energy redistribution with the inner EC for propagations longer than $2 \mu\text{m}$ in the probed energy range. Therefore, the observed small discrepancies could also result from the finite $0.8 \mu\text{m}$ propagation length.

Overall, we demonstrate that QPCs in the QHR are tunable electrical beam splitters for one-dimensional fermions, i.e. rigid edge channel displacements, *i*) by comparing the energy distribution at a QPC output with predictions of the scattering approach⁵, and *ii*) by showing that internal edge channel modes are not excited. This does not only rule out non-ideal QPC behaviors to explain the surprising phenomena observed on electronic Mach-Zehnder^{8,15,16,17}. It also establishes a solid ground for future quantum information applications with edge states. Finally, an essential part of this work is the demonstration of a new technique to measure the fundamental energy distribution function. It makes $f(E)$ accessible for most systems where quantum dots can be realized. We expect it will trigger many new experiments dealing with heat transport, out-of-equilibrium physics and quantum decoherence.

* email: frederic.pierre@lpn.cnrs.fr

¹ Klitzing, K. v., Dorda, G. & Pepper, M. New Method for

High-Accuracy Determination of the Fine-Structure Constant Based on Quantized Hall Resistance. *Phys. Rev. Lett.*

- 45, 494–497 (1980).
- ² Fertig, H. A. A view from the edge. *Physics* **2**, 15 (2009).
 - ³ Halperin, B. I. Quantized Hall conductance, current-carrying edge states, and the existence of extended states in a two-dimensional disordered potential. *Phys. Rev. B* **25**, 2185–2190 (1982).
 - ⁴ Wen, X.-G. Theory of the edges states in fractional quantum Hall effects. *Int. J. Mod. Phys B* **6**, 1711–1762 (1992).
 - ⁵ Büttiker, M. Absence of backscattering in the quantum Hall effect in multiprobe conductors. *Phys. Rev. B* **38**, 9375–9389 (1988).
 - ⁶ Ionicioiu, R., Amaratunga, G. & Udrea, F. Quantum Computation with Ballistic Electrons. *Int. J. Mod. Phys. B* **15**, 125 (2001).
 - ⁷ Stace, T. M., Barnes, C. H. W. & Milburn, G. J. Mesoscopic One-Way Channels for Quantum State Transfer via the Quantum Hall Effect. *Phys. Rev. Lett.* **93**, 126804 (2004).
 - ⁸ Ji, Y. *et al.* An electronic Mach-Zehnder interferometer. *Nature* **422**, 415–418 (2003).
 - ⁹ Fève, G. *et al.* An On-Demand Coherent Single-Electron Source. *Science* **316**, 1169–1172 (2007).
 - ¹⁰ Samuelsson, P., Sukhorukov, E. V. & Büttiker, M. Two-Particle Aharonov-Bohm Effect and Entanglement in the Electronic Hanbury Brown-Twiss Setup. *Phys. Rev. Lett.* **92**, 026805 (2004).
 - ¹¹ Ol’khovskaya, S., Splettstoesser, J., Moskalets, M. & Büttiker, M. Shot Noise of a Mesoscopic Two-Particle Collider. *Phys. Rev. Lett.* **101**, 166802 (2008).
 - ¹² Chklovskii, D. B., Shklovskii, B. I. & Glazman, L. I. Electrostatics of edge channels. *Phys. Rev. B* **46**, 4026–4034 (1992).
 - ¹³ Aleiner, I. L. & Glazman, L. I. Novel edge excitations of two-dimensional electron liquid in a magnetic field. *Phys. Rev. Lett.* **72**, 2935–2938 (1994).
 - ¹⁴ Neder, I. *et al.* Interference between two indistinguishable electrons from independent sources. *Nature* **448**, 333–337 (2007).
 - ¹⁵ Roulleau, P. *et al.* Direct Measurement of the Coherence Length of Edge States in the Integer Quantum Hall Regime. *Phys. Rev. Lett.* **100**, 126802 (2008).
 - ¹⁶ Litvin, L. V., Tranitz, H. P., Wegscheider, W. & Strunk, C. Decoherence and single electron charging in an electronic Mach-Zehnder interferometer. *Phys. Rev. B* **75**, 033315 (2007).
 - ¹⁷ Bieri, E. *et al.* Finite-bias visibility dependence in an electronic Mach-Zehnder interferometer. *Phys. Rev. B* **79**, 245324 (2009).
 - ¹⁸ Tsui, D. C., Stormer, H. L. & Gossard, A. C. Two-Dimensional Magnetotransport in the Extreme Quantum Limit. *Phys. Rev. Lett.* **48**, 1559–1562 (1982).
 - ¹⁹ MacDonald, A. H., Yang, S. R. E. & Johnson, M. D. Quantum dots in strong magnetic fields: Stability criteria for the maximum density droplet. *Aust. J. Phys.* **46**, 345 (1993).
 - ²⁰ Chamon, C. d. C. & Wen, X. G. Sharp and smooth boundaries of quantum Hall liquids. *Phys. Rev. B* **49**, 8227–8241 (1994).
 - ²¹ Chang, A. M., Pfeiffer, L. N. & West, K. W. Observation of Chiral Luttinger Behavior in Electron Tunneling into Fractional Quantum Hall Edges. *Phys. Rev. Lett.* **77**, 2538–2541 (1996).
 - ²² Roddaro, S., Pellegrini, V., Beltram, F., Pfeiffer, L. N. & West, K. W. Particle-Hole Symmetric Luttinger Liquids in a Quantum Hall Circuit. *Phys. Rev. Lett.* **95**, 156804 (2005).
 - ²³ Conti, S. & Vignale, G. Collective modes and electronic spectral function in smooth edges of quantum hall systems. *Phys. Rev. B* **54**, R14309–R14312 (1996).
 - ²⁴ Han, J. H. & Thouless, D. J. Dynamics of compressible edge and bosonization. *Phys. Rev. B* **55**, R1926–R1929 (1997).
 - ²⁵ Yang, K. Field Theoretical Description of Quantum Hall Edge Reconstruction. *Phys. Rev. Lett.* **91**, 036802 (2003).
 - ²⁶ Zülicke, U. & MacDonald, A. H. Periphery deformations and tunneling at correlated quantum Hall edges. *Phys. Rev. B* **60**, 1837–1841 (1999).
 - ²⁷ Pothier, H., Guéron, S., Birge, N. O., Esteve, D. & Devoret, M. H. Energy Distribution Function of Quasiparticles in Mesoscopic Wires. *Phys. Rev. Lett.* **79**, 3490–3493 (1997).
 - ²⁸ Anthore, A., Pierre, F., Pothier, H. & Esteve, D. Magnetic-Field-Dependent Quasiparticle Energy Relaxation in Mesoscopic Wires. *Phys. Rev. Lett.* **90**, 076806 (2003).
 - ²⁹ Heiblum, M., Nathan, M. I., Thomas, D. C. & Knoedler, C. M. Direct Observation of Ballistic Transport in GaAs. *Phys. Rev. Lett.* **55**, 2200–2203 (1985).
 - ³⁰ Granger, G., Eisenstein, J. P. & Reno, J. L. Observation of Chiral Heat Transport in the Quantum Hall Regime. *Phys. Rev. Lett.* **102**, 086803 (2009).
 - ³¹ Averin, D. V., Korotkov, A. N. & Likharev, K. K. Theory of single-electron charging of quantum wells and dots. *Phys. Rev. B* **44**, 6199–6211 (1991).
 - ³² Kouwenhoven, L. P. *et al.* Electron transport in quantum dots. In *Mesoscopic Electron Transport Series E: Applied Sciences* (eds. Sohn, L. L., Kouwenhoven, L. P. & Schön, G.), vol. 345, 105–214 (Kluwer Academic, 1997).
 - ³³ van der Vaart, N. C. *et al.* Resonant Tunneling Through Two Discrete Energy States. *Phys. Rev. Lett.* **74**, 4702–4705 (1995).
 - ³⁴ van Wees, B. J. *et al.* Anomalous integer quantum Hall effect in the ballistic regime with quantum point contacts. *Phys. Rev. Lett.* **62**, 1181–1184 (1989).
 - ³⁵ Gramespacher, T. & Büttiker, M. Local densities, distribution functions, and wave-function correlations for spatially resolved shot noise at nanocontacts. *Phys. Rev. B* **60**, 2375–2390 (1999).

Acknowledgments

The authors gratefully acknowledge discussions with M. Büttiker, P. Degiovanni, C. Glattli, P. Joyez, A.H. MacDonald, F. Portier, H. Pothier, P. Roche, G. Vignale. This work was supported by the ANR (ANR-05-NANO-028-03).

Author contributions

Experimental work and data analysis: C.A., H.I.S. and F.P.; nano-fabrication: C.A. and F.P. with inputs from D.M.; heterojunction growth: A.C. and U.G.; theoretical analysis and manuscript preparation: F.P. with inputs from coauthors; project planning and supervision: F.P.

Additional information

dressed to F.P.

Supplementary Information accompanies this paper.
Correspondence and requests for materials should be ad-

Supplementary Information for 'Non-Equilibrium Edge Channel Spectroscopy in the Integer Quantum Hall Regime'

C. Altimiras,¹ H. le Sueur,¹ U. Gennser,¹ A. Cavanna,¹ D. Mailly,¹ and F. Pierre¹

¹CNRS, Laboratoire de Photonique et de Nanostructures (LPN) - Phynano team, route de Nozay, 91460 Marcoussis, France

(Dated: October 14, 2009)

I. EXPANDED DISCUSSION ON ENERGY AND HEAT TRANSPORT BY EDGE EXCITATIONS

In this section, after a schematic summary of the experimental principle, we first detail how the energy within the probed electronic excitations can be extracted from the energy distribution function $f(E)$ and we define a generalized temperature T_{qp} for non-equilibrium situations. Second, we detail the link between energy within a system of 1D chiral fermions, such as the 'quasiparticles' (i.e. the rigid edge channel displacement excitations), and energy transport. In this case, distribution function and heat current are directly related, without any sample specific parameters. Third, we extract from general power balance considerations the total excess energy current carried by all edge excitations. It is compared to the energy current carried only by the probed quasiparticles. This permits us to rule out any contribution of internal modes to the energy transport within our experimental accuracy.

A. Schematic summary of experiment principle

Figure 1 recapitulates the logical architecture that permits us to rule out the excitation of internal EC states and to show that QPCs obey the scattering model for quasiparticles¹. This demonstrates the quantum optics analogy, regarding energy transport, between a QPC and a tunable beam splitter for quasiparticles.

The hypothesis H1 relies on the linear I-V characteristic for tunnel contacts that is mostly observed (including here) in the integer QHR^{2,3,4,5,6}. The hypothesis H2 holds for each edge channel's quasiparticle branch according to^{2,3,4,7}. Note that the hydrodynamic approach considers specifically rigid EC displacements⁷. The hypothesis H3 is a prediction for internal EC modes^{2,3,4,8}.

B. Energy density of non-equilibrium fermions

At equilibrium and temperature T , the energy distribution function $f(E)$ is a Fermi function and the typical energy of electronic excitations is $k_B T$. In non-equilibrium situations, the distribution function is in general not a Fermi function. Nevertheless, the energy density E_{qp} within a system of fermionic quasiparticles can

Working hypothesis

H1: Tunnel contacts do not couple to internal EC modes

H2: "Quasiparticles" can be described as 1D chiral fermions (quasiparticles = rigid EC displacement excitations)

H3: Internal EC modes are propagative

Implications of hypothesis

H1 \Rightarrow **I1:** $f(E)$ measured with a tunnel coupled QD is that of quasiparticles

H2 + I1 \Rightarrow **I2:** Quasiparticle heat current J_E^{qp} given by Eq. 4

H3 \Rightarrow **I3:** If \exists excited internal states at QPC then this implies excess $J_E^{qp} <$ excess edge excitations heat current J_E

Experimental observations

E1: Measured $f(E)$ complies with Eq. 1

E2 (using **I2**): Excess $J_E^{qp} \sim$ excess J_E

Conclusions

E1 + I1 \Rightarrow **C1:** Quasiparticles $f(E)$ obey the scattering model of QPCs

E2 + I3 \Rightarrow **C2:** Internal modes are not excited at the QPC

C1 + C2 \Rightarrow **C3:** Regarding energy transport, QPCs in int. QHR are electrical analogues for quasiparticles of tunable beam splitters

Figure 1: **Schematic summary of experiment principle.**

be obtained from their energy distribution:

$$\begin{aligned}
 E_{qp} &= \nu \int_{-\infty}^{\mu} (\mu - E)(1 - f(E))dE \\
 &\quad + \nu \int_{\mu}^{\infty} (E - \mu)f(E)dE, \\
 &= \nu \int (E - \mu)\delta f(E)dE, \tag{1}
 \end{aligned}$$

with ν the density of states per unit length and energy, here assumed constant for energies near the local electrochemical potential μ ; and $\delta f(E) = f(E) - \theta(\mu - E)$, with $\theta(E)$ the step function, corresponding to variations in the energy distribution relative to the filled Fermi sea. The second line and the right-hand side of the first line correspond to the energy density contribution of, respectively, electron and hole like quasiparticles. In the important case of a Fermi function at temperature T , the energy density obtained from Supplementary equation 1 is the

standard textbook value⁹:

$$E_{qp} = \frac{\pi^2}{6} \nu (k_B T)^2. \quad (2)$$

In practice, it is more convenient to use the electronic temperature T_{qp} generalized to non-equilibrium situations, which is independent of the density of states, rather than the energy density E_{qp} :

$$T_{qp} \equiv \sqrt{\frac{6(E_{qp}/\nu)}{\pi^2}} / k_B. \quad (3)$$

The energy density and generalized electronic temperature can be computed analytically for the ‘double step’ energy distributions detailed by Eq. (2). One finds:

$$E_{qp}/\nu = \frac{(\pi k_B T)^2}{6} + \tau(1-\tau) \frac{(e\delta V_D)^2}{2}, \quad (4)$$

$$T_{qp} = \sqrt{T^2 + 3\tau(1-\tau) \left(\frac{e\delta V_D}{\pi k_B} \right)^2}. \quad (5)$$

C. Energy transport by 1D chiral fermions

We expect from the rigid displacement model^{2,3,4,5} supported by tunneling density of states experiments, that the energy distribution, measured here with a weakly coupled quantum dot, is that of rigid displacement excitations (the quasiparticles) and not of internal edge channel excitations. Moreover, it was shown that the quasiparticles of each edge channel can be mapped onto a branch of 1D chiral fermions^{2,3,4,7}. Therefore, the measured energy current J_E^{qp} along an edge channel corresponds to that of quasiparticles and reads:

$$J_E^{qp} = v E_{qp} = \frac{\pi^2}{6h} (k_B T_{qp})^2, \quad (6)$$

with v the drift velocity and h the Plank constant. Note first that the right-hand side expression of heat current holds even if the density of states ν depends on energy, as long as the very robust 1D velocity-density of states cancellation $v\nu = 1/h$ is obeyed¹⁰. Second, as expected the above expression obeys the Wiedemann-Franz law. Third, we point out that the energy flow is directly given by the generalized temperature T_{qp} , without any sample specific parameters. Therefore, by measuring the energy distribution function in our experiment, we probe quantitatively the quasiparticle energy current.

Assuming the quasiparticle distribution function is given by Equation (2), the corresponding energy flow is:

$$J_E^{qp} = \frac{\pi^2}{6h} (k_B T)^2 + \tau(1-\tau) \frac{(e\delta V_D)^2}{2h}. \quad (7)$$

D. Excess energy transport by all edge excitations and comparison with that by quasiparticles

We consider the simplified circuit at filling factor 1 (one edge channel) shown in Supplementary figure 2.

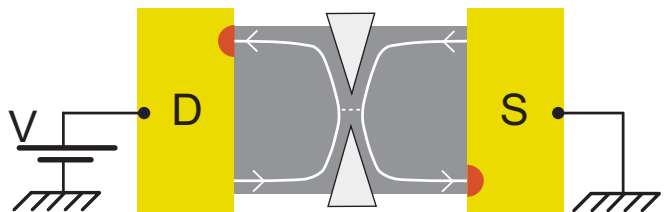


Figure 2: **Simplified schematic circuit used for power balance considerations.** The Landau level filling factor is here set to one. The edge channel is shown as a white line and the propagation direction of electronic excitations is indicated by an arrow. The dissipated power $V^2 G_{QPC} = V^2 \tau e^2 / h$ is injected into the source (S) and drain (D) electrodes by the corresponding incoming edge channels.

Here, the total power $P = V^2 \tau e^2 / h$, with τ the quantum point contact transmission, is dissipated in the source (S) and drain (D) electrodes (nearby the hot spots shown as red areas in Supplementary figure 2, see e.g.¹¹). It can be decomposed into two contributions:

$$P = V^2 \tau e^2 / h = P_{\delta\mu} + P_{edge}. \quad (8)$$

The first one ($P_{\delta\mu}$) corresponds to the energy injected into the drain and source electrodes due to the electrochemical potential difference $\delta\mu$ between electrode and corresponding incoming edge. The edge electrochemical potential is defined as that of a floating electrode inserted in its path, in the spirit of the ‘measurement reservoir’ model (see e.g.¹⁰). At unity transmission $\tau = 1$, this ‘electrochemical power’ is the only contribution to the dissipated power $P_{\delta\mu}(\tau = 1) = P = (eV)^2 / h$. In general, the electrochemical power injected by each edge in its output electrode is $(\delta\mu)^2 / 2h$. At arbitrary transmission τ , the electrochemical potential difference at the input of both the source and drain electrodes is $|\delta\mu| = \tau e|V|$ and one finds:

$$P_{\delta\mu} = (\tau eV)^2 / h. \quad (9)$$

The second contribution $P_{edge} = 2(J_E^{in} - J_E^{out})$ corresponds to the difference between the incoming J_E^{in} and outgoing J_E^{out} energy current carried on by *all edge excitations*, respectively in and out the corresponding electrode. The factor two here accounts for the two electrodes. Note that P_{edge} corresponds to the amount of energy that would be absorbed by two floating reservoirs inserted along the path of the edges incoming to source and drain electrodes and thermalized at the same temperature as their corresponding electrode. This contribution vanishes at zero transmission and also at unity transmission, as long as the drain and source electrodes are at the same temperature since in that case $J_E^{in} = J_E^{out}$. At intermediate transmissions, P_{edge} is obtained from Supplementary equations 8 and 9:

$$P_{edge} = P - P_{\delta\mu} = \tau(1-\tau) \frac{(e\delta V_D)^2}{h}. \quad (10)$$

This last quantity is identical to the one obtained from the double step distribution function (using J_E^{in} given by Supplementary equation 7 and $J_E^{out} = \frac{\pi^2}{6h}(k_B T)^2$). Therefore the observed agreement between measured quasiparticle $f(E)$ and the prediction of Eq. 2 already implies that the excess energy current is carried on by quasiparticles and not internal edge channel modes. However, the most straightforward evidence is to extract the energy current directly from the measured quasiparticle energy distribution function using Supplementary equations 1, 3 and 6. The internal modes being propagative, the observation that excess quasiparticle energy current and full excess edge current are similar (see Figures 3d and 4d) implies internal edge channel states are not excited by a voltage biased QPC of arbitrary transmission within our experimental accuracy.

II. SUPPLEMENTARY DATA

In this section we present supplementary data regarding cooldowns two and three, that were not shown in the article.

The quantum dot calibration data are shown in Supplementary figure 3.

Data obtained in cooldown two with a fixed bias voltage $\delta V_D = -36 \mu\text{V}$ and several values of the QPC conductance are shown in Supplementary figure 4. These data correspond to symbols (+) in Figure 3c,d. Note that here V_{D2} and the inner edge channel potential are set to $-129 \mu\text{V}$.

Data obtained in cooldown three with a fixed QPC conductance $G_{QPC} \simeq 0.5e^2/h$ and several values of the QPC voltage bias δV_D are shown in Supplementary figure 5. As for cooldown one, V_{D2} and the inner edge channel potential are here fixed to $-88 \mu\text{V}$.

III. SUPPLEMENTARY INFORMATION ON METHODS

A. Measured sample and experimental techniques

The sample was realized in a standard GaAs/Ga(Al)As two dimensional electron gas 105 nm below the surface, of density $2 \cdot 10^{15} \text{ m}^{-2}$, Fermi energy 80 K and mobility $250 \text{ m}^2\text{V}^{-1}\text{s}^{-1}$. Note that the GaAs/Ga(Al)As heterojunction used here is the same one as that used formerly to perform the Mach-Zehnder experiments with edge states reported in^{12,13}. The silicon (dopant) concentration in the heterojunction was adjusted to optimize the Hall resistance quantization.

Conductance measurements were performed in a dilution refrigerator of base temperature 30 mK. All measurement lines were filtered by commercial π -filters at the top of the cryostat. At low temperature, the lines were carefully filtered and thermalized by arranging them as

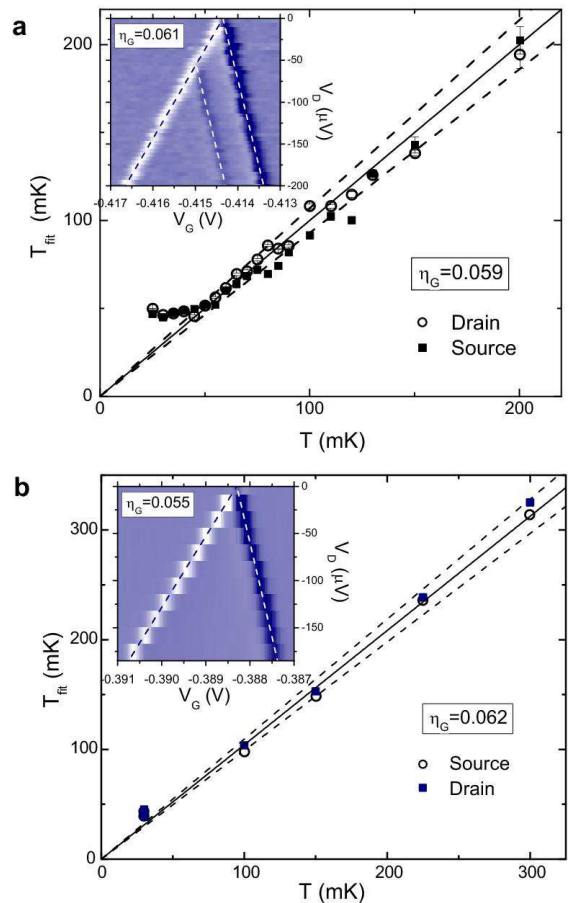


Figure 3: **Quantum dot calibration in cooldowns two and three.** This figure complements Figure 2 that focused on cooldown one. (a) and (b) are calibration data for cooldowns two and three, respectively. Errors in T_{fit} within $\pm 7\%$ for cooldown two (a) and within $\pm 5\%$ for cooldown three (b) are enclosed between the black dashed lines. Note that an additional QD level of relative energy $-56 \mu\text{eV}$ for cooldown two is visible in the top left inset of (a).

1 m long resistive twisted pairs ($300 \Omega/\text{m}$) inserted inside $260 \mu\text{m}$ inner diameter CuNi tubes tightly wrapped around a copper plate screwed to the mixing chamber. The sample was further protected from spurious high energy photons by two shields, both at base temperature.

The sample was current biased by a voltage source in series with a $10 \text{ M}\Omega$ or $100 \text{ M}\Omega$ polarization resistance at room temperature. Taking advantage of the well defined quantum Hall resistance ($12.906 \text{ k}\Omega$), currents across the sample were converted on-chip into voltages and measured with low noise room temperature voltage amplifiers. To limit artifacts by slowly moving charges nearby the QD, we systematically measured several successive gate voltage sweeps $I_{QD}(V_G)$, checked that the data fall on top of each other, and verified that the sum rule $\int (\partial I_{QD} / \partial V_G) dV_G \simeq 0$ is obeyed.

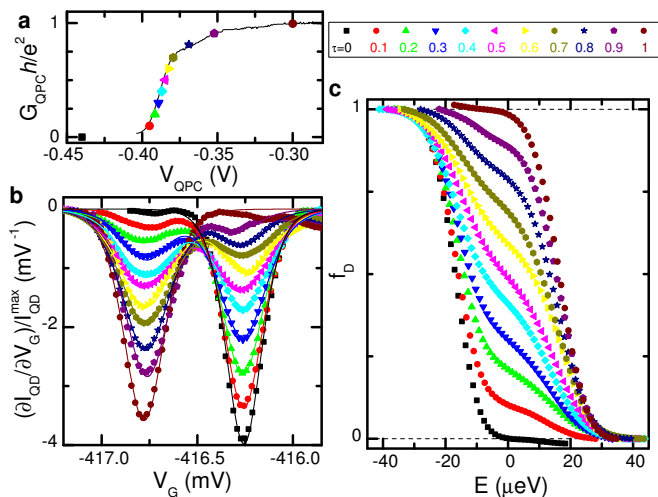


Figure 4: **Spectroscopy of an edge channel tuned out-of-equilibrium with the conductance of a QPC in cooldown two.** The QPC's voltage bias is here fixed to $\delta V_D \equiv V_{D1} - V_{D2} = -36 \mu\text{V}$. **a**, Measured G_{QPC} versus V_{QPC} applied to the lower left metal gate in Figure 1c. Symbols are data points obtained during the corresponding EC spectroscopy. The continuous line was measured with $\delta V_D = 0$. **b**, Measured $\partial I_{\text{QD}}/\partial V_G$ (symbols) for the QD-drain contribution (data have been aligned in V_G and normalized to $I_{\text{QD}}^{\text{max}}$). Continuous lines are fits assuming $f_D(E)$ is the weighted sum of two Fermi functions. The detailed set of used fit parameters is given in Supplementary table III. **c**, Energy distributions obtained by integrating the data in (b) and using $\eta_G = 0.059$.

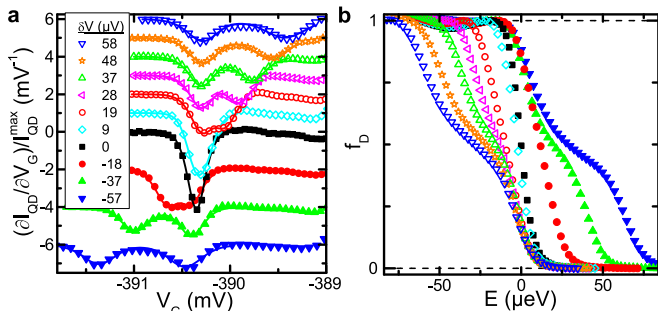


Figure 5: **Spectroscopy of an edge channel tuned out-of-equilibrium with the voltage across a QPC in cooldown three.** The QPC's conductance is here fixed to $G_{\text{QPC}} = 0.5e^2/h$. **a**, Measured $\partial I_{\text{QD}}/\partial V_G$ (symbols) for the QD-drain contribution. Data have been shifted vertically for clarity, and horizontally to align the peak corresponding to the fixed potential V_{D2} . Continuous lines are fits assuming $f_D(E)$ is the weighted sum of two Fermi functions (see Supplementary table IV). **b**, Energy distributions obtained by integrating the data in (a) and using $\eta_G = 0.062$.

B. Quantum dot theoretical model

The QD modeling follows the master equation approach for incoherent sequential tunneling. The derivation detailed in¹⁴ stays valid for non-Fermi distribution

functions. To obtain the simple expression of Equation 1 we assumed only one QD level contributes to I_{QD} , and neglected the energy dependence of the electrodes tunneling density of states and of the tunnel rates in and out the QD. In practice, the validity of these hypotheses are checked with the non-linear QD characterization and by comparing mixing chamber temperatures with fit temperatures obtained within this framework (see Figure 2 and Supplementary figure 3). Note that, beyond sequential tunneling, a similar relationship between I_{QD} and $f_{S,D}$ holds in the resonant transport regime but with distribution functions artificially smoothed by the energy width of the QD level.

C. Experimental procedures

1. Extraction of the energy distribution function

The distribution functions $f(E)$ are obtained by integrating with V_G the normalized data $-(\partial I_{\text{QD}}/\partial V_G)/I_{\text{QD}}^{\text{max}}$ from a charge stability zone ($I_{\text{QD}} = 0$) on the negative side up to $V_G = -(E - E_0)/e\eta_G$.

2. Extraction of the electrochemical potential

The electrochemical potential μ enters in the evaluation of the energy density (Supplementary equation 1), and consequently in the heat current J_E^{qp} and in the generalized quasiparticle temperature T_{qp} . The parameter μ is here obtained very directly from the measured $f(E)$ using

$$\mu = E_{\text{min}} + \int_{E_{\text{min}}}^{E_{\text{max}}} f(E) dE, \quad (11)$$

with E_{min} (E_{max}) an energy under (above) which we assume $f(E) = 1$ ($f(E) = 0$). Note that μ is obtained up to the same unknown constant offset E_0 as $f(E)$, however this has no impact since only the difference $E - \mu$ plays a role.

3. Estimation of uncertainties on the lever arm η_G

Uncertainties in the gate voltage-to-energy lever arm conversion factor η_G are mostly responsible for our error bars on energy related quantities (e.g. Figs. 3d and 4c,d).

This parameter is extracted from two independent calibration procedures: First, we perform a non-linear characterization of the QD¹⁵ and extract η_G from the slopes of the Coulomb diamond $\partial I_{\text{QD}}/\partial V_G(V_G, V_D)$ (hereafter called procedure 1). Second, we measure $\partial I_{\text{QD}}/\partial V_G(V_G)$ at several temperatures and extract η_G from the scaling between fit temperatures (using Fermi functions in

Equation 1) and measured mixing chamber temperatures (hereafter called procedure 2).

In procedure 1, uncertainties on η_G are obtained from the change in slopes corresponding to displacements equal to the full width at half maximum of the peaks at the highest drain-source voltage. This gives $\eta_G = 0.052 \pm 9\%$, $0.062 \pm 8\%$ and $0.055 \pm 9\%$ for, respectively, cooldowns one, two and three. Note that these uncertainties correspond to plus and minus the full width at half maximum corresponding to the effective electronic temperature 50 mK (i.e. $0.05 \times 3.5k_B/e \simeq 15 \mu\text{V}$) divided by the maximum drain voltage V_D applied.

In procedure 2, uncertainties in η_G are obtained from the dispersion in fit temperatures T_{fit} around measured temperatures T of the dilution refrigerator mixing chamber. We evaluate roughly the uncertainty by finding the range of η_G that permits us to account for most T_{fit} at $T > 50$ mK. The reader can get a direct idea of the used uncertainties in Figure 2 and Supplementary figure 3, where the expected fit temperatures using the considered extremal values of η_G are shown as dashed lines. This gives $\eta_G = 0.057 \pm 10\%$, $0.059 \pm 7\%$ and $0.062 \pm 5\%$ for, respectively, cooldowns one, two and three.

In the article, we have chosen to use the values of η_G and the associated uncertainties extracted using procedure 2, in the same experimental configuration as to measure unknown $f(E)$ s.

4. Estimation of error bars

The error bars in the figures take into account the finite signal to noise and reproducibility (i.e. the standard error in the average value), and, if it applies, uncertainties in the lever arm.

Regarding the finite signal to noise and reproducibility our approach is very straightforward. We perform a statistical analysis on the considered quantity extracted from up to a hundred different V_G sweeps in the exact same experimental configuration. The corresponding standard error is then plus/minus the mean deviation per sweep divided by the square root of the number of sweeps. This is the only contribution for the parameter τ_{fit} whose typical error bars are found to be about 0.02, small compared to the symbol size in Fig. 3c. Note that in practice, we acquired the large number of sweeps necessary for an accurate statistical analysis in only a few realizations per experiment. In other realizations of a given experiment (i.e. when changing only the QPC conductance or the applied voltage bias), we assumed that the observed mean deviation per sweep is unchanged and estimate the standard error using the corresponding number of sweeps (generally more than five).

It turns out that, except for the immune τ_{fit} , error bars are mostly dominated by uncertainties on the lever arm η_G and therefore are proportional to the overall energy (namely, T_{qp} or δV_D). Indeed, the standard error on T_{qp} was always found smaller than 1 mK for cooldowns

| $G_{QPC} (e^2/h)$ | τ_{fit} | $T_{D1}(K)$ | $T_{D2}(K)$ |
|-------------------|--------------|-------------|-------------|
| 0 | 0 | 0.042 | 0.042 |
| 0.15 | 0.18 | 0.158 | 0.042 |
| 0.26 | 0.25 | 0.078 | 0.046 |
| 0.35 | 0.33 | 0.071 | 0.049 |
| 0.43 | 0.42 | 0.067 | 0.050 |
| 0.51 | 0.48 | 0.062 | 0.054 |
| 0.59 | 0.58 | 0.064 | 0.054 |
| 0.59 | 0.61 | 0.067 | 0.056 |
| 0.65 | 0.65 | 0.062 | 0.056 |
| 0.72 | 0.73 | 0.061 | 0.053 |
| 0.78 | 0.77 | 0.056 | 0.059 |
| 0.88 | 0.86 | 0.053 | 0.073 |
| 1 | 1 | 0.045 | 0.045 |

Table I: **Summary of parameters used to fit the data shown in Figure 3b (cooldown one).** The conductance G_{QPC} is measured. Note that near zero and full transmission, the fit temperature of the small corresponding peak is not very significant. In order to focus on the fit parameter τ_{fit} , we chose to fix $\eta_G \delta V_G = 30 \mu\text{V}$. If $\eta_G \delta V_G$ is set free, we find values within $30 \pm 1 \mu\text{V}$, except at $G_{QPC} = 0.9e^2/h$ where $\eta_G \delta V_G = 39 \mu\text{V}$. Note that τ_{fit} is not affected more than ± 0.03 by whether $\eta_G \delta V_G$ is fixed or free.

| $\delta V_D (\mu\text{V})$ | $T_{D1} (K)$ | $T_{D2}(K)$ | $\eta_G \delta V_G (\mu\text{V})$ |
|----------------------------|--------------|-------------|-----------------------------------|
| -18 | 0.049 | 0.049 | -12 |
| 0 | 0.040 | 0.040 | 0 |
| 18 | 0.048 | 0.045 | 13 |
| 27 | 0.054 | 0.054 | 20 |
| 36 | 0.061 | 0.056 | 29 |
| 45 | 0.074 | 0.063 | 38 |
| 54 | 0.076 | 0.073 | 46 |

Table II: **Summary of parameters used to fit the data shown in Figure 4b (cooldown one).** Here δV_D is the applied voltage bias and the parameter τ_{fit} is set to the measured $G_{QPC}h/e^2 = 0.58$.

one and three, and 4 mK for cooldown two. Nevertheless, the full error bars shown in figures include both contributions, taken as independent from each other.

5. Fit procedures

We fitted the measured $(\partial I_{QD}/\partial V_G)/I_{QD}^{max}$ using Equations 1 and 2, with Fermi functions for f_{D1} and f_{D2} . The full set of fit parameters is not only constituted of τ_{fit} and $\eta_G \delta V_G$ shown in Figures 3c and 4c, respectively. It also includes the temperatures T_{D1} and T_{D2} of the corresponding Fermi functions. We recapitulate the full set of used fit parameters in Supplementary tables I, II, III and IV.

| G_{QPC} (e^2/h) | τ_{fit} | $T_{D1} = T_{D2}$ (K) | $\eta_G \delta V_G$ (μV) |
|-----------------------|--------------|-----------------------|---------------------------------|
| 0 | 0 | 0.043 | -36 |
| 0.10 | 0.08 | 0.046 | -30 |
| 0.20 | 0.18 | 0.050 | -31 |
| 0.30 | 0.28 | 0.057 | -30 |
| 0.40 | 0.41 | 0.062 | -30 |
| 0.50 | 0.49 | 0.065 | -30 |
| 0.60 | 0.61 | 0.063 | -31 |
| 0.70 | 0.71 | 0.063 | -30 |
| 0.81 | 0.80 | 0.057 | -30 |
| 0.91 | 0.89 | 0.054 | -28 |
| 1 | 1 | 0.049 | -36 |

Table III: **Summary of parameters used to fit the data shown in Supplementary figure 4b (cooldown 2).** The conductance G_{QPC} is measured. The applied QPC voltage bias is here $\delta V_D = -36 \mu V$. The lever arm is $\eta_G = 0.059$.

| δV_D (μV) | T_{D1} (K) | T_{D2} (K) | $\eta_G \delta V_G$ (μV) |
|--------------------------|--------------|--------------|---------------------------------|
| -57 | 0.089 | 0.077 | -56 |
| -37 | 0.073 | 0.061 | -36 |
| -18 | 0.055 | 0.054 | -15 |
| 0 | 0.044 | 0.044 | 0 |
| 9 | 0.046 | 0.043 | 7 |
| 19 | 0.057 | 0.052 | 15 |
| 28 | 0.064 | 0.055 | 24 |
| 37 | 0.073 | 0.060 | 32 |
| 48 | 0.088 | 0.070 | 44 |
| 58 | 0.094 | 0.080 | 53 |

Table IV: **Summary of parameters used to fit the data shown in Supplementary figure 5a (cooldown 3).** Here δV_D is the applied voltage bias and the parameter τ_{fit} is set to the measured $G_{QPC} h/e^2 = 0.5$. The lever arm is $\eta_G = 0.062$.

IV. SUPPLEMENTARY DISCUSSION REGARDING DEVIATIONS BETWEEN DATA AND FREE 1D CHIRAL FERMIONS THEORY

In this section, we discuss two possible explanations of the observed deviations between the data and the free 1D chiral fermions predictions that can be seen in Figures 3d, 4c and 4d. The first one relies on additional active quantum dot levels. The second one on energy redistribution with the inner edge channel.

A. Effect of additional quantum dot levels

In the presence of more than one active quantum dot level, the straightforward Equation 1 does not hold. In the sequential tunneling regime, the master equation approach applies¹⁵. This can result in non-intuitive phenomena. In particular, it was shown that the gate voltage position of a Coulomb peak can be shifted by about its width when the temperature changes¹⁶. We found a similar phenomenon could change the gate voltage separation between the two dips observed in presence of a double step energy distribution.

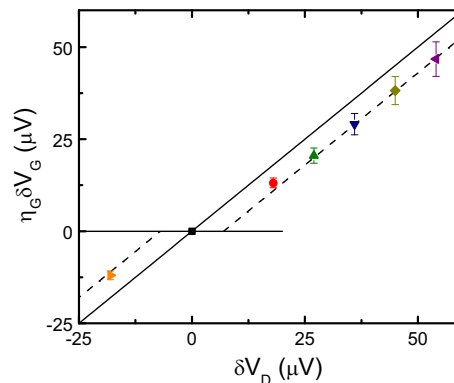


Figure 6: **Possible explanation with additional QD levels of observed small deviations on cooldown one.** Data shown as symbols are those obtained in cooldown one and also displayed in Figure 4c. Dashed lines correspond to the slope predicted by $\eta_G = 0.057$ but shifted horizontally by $\pm 7 \mu V$. Such shifts are compatible with the presence of a second active QD level located at $\varepsilon \approx -10 \mu eV$, below the first level.

By solving the master equation with non-equilibrium energy distributions, using a slightly modified version of the code provided by¹⁶, and with a second level of energy ε nearby the first active level, we could reproduce the observed difference between $\eta_G \delta V_G$ and δV_D shown in Figure 4d and Supplementary figure 6. Such second level for cooldown one is not visible in the top left inset of Figure 2 but its existence is suggested by data taken in slightly different conditions (not shown) and by the observed $T_S > T_D$ at $T = 30$ mK (see Figure 2). The presence of such a level can reduce $|\delta V_G|$ by a constant offset for $|e\delta V_D| > |\varepsilon|$ if asymmetrically coupled to the source and drain electrodes. Supplementary figure 6 shows $\eta_G \delta V_G$ extracted from cooldown one (data also shown in Figure 4c) together with dashed lines of slopes as expected from $\eta_G = 0.057$ but offset by $\pm 7 \mu V$ which is compatible with a second level located at $\varepsilon \approx -10 \mu eV$, below the first level.

B. Effect of energy redistribution with inner edge channel

More recent data that we obtained using the same experimental configuration show that an energy redistribution exists between the outer and inner edge channels on length scales larger than $2 \mu m$ ¹⁷. This effect, although probably small for the short $0.8 \mu m$ propagation length considered here, could explain the also small deviation observed between the free 1D chiral fermions model and our data in Figures 3d and 4d. Another indication that energy relaxation along the edge is not fully negligible is the observed increase in the fit temperatures T_{D1} and T_{D2} with injected power (see Supplementary tables I, II, III and IV).

-
- ¹ Gramespacher, T. & Büttiker, M. Local densities, distribution functions, and wave-function correlations for spatially resolved shot noise at nanocontacts. *Phys. Rev. B* **60**, 2375–2390 (1999).
- ² Aleiner, I. L. & Glazman, L. I. Novel edge excitations of two-dimensional electron liquid in a magnetic field. *Phys. Rev. Lett.* **72**, 2935–2938 (1994).
- ³ Conti, S. & Vignale, G. Collective modes and electronic spectral function in smooth edges of quantum hall systems. *Phys. Rev. B* **54**, R14309–R14312 (1996).
- ⁴ Han, J. H. & Thouless, D. J. Dynamics of compressible edge and bosonization. *Phys. Rev. B* **55**, R1926–R1929 (1997).
- ⁵ Zülicke, U. & MacDonald, A. H. Periphery deformations and tunneling at correlated quantum Hall edges. *Phys. Rev. B* **60**, 1837–1841 (1999).
- ⁶ Yang, K. Field Theoretical Description of Quantum Hall Edge Reconstruction. *Phys. Rev. Lett.* **91**, 036802 (2003).
- ⁷ Wen, X.-G. Theory of the edges states in fractional quantum Hall effects. *Int. J. Mod. Phys B* **6**, 1711–1762 (1992).
- ⁸ Chamon, C. d. C. & Wen, X. G. Sharp and smooth boundaries of quantum Hall liquids. *Phys. Rev. B* **49**, 8227–8241 (1994).
- ⁹ Pines, D. & Nozières, P. *The Theory of Quantum Liquids* (Perseus Books, 1966).
- ¹⁰ Sivan, U. & Imry, Y. Multichannel Landauer formula for thermoelectric transport with application to thermopower near the mobility edge. *Phys. Rev. B* **33**, 551–558 (1986).
- ¹¹ Klass, U., Dietsche, W., von Klitzing, K. & Ploog, K. Imaging of the dissipation in quantum-Hall-effect experiments. *Z. Phys. B: Condens. Matter* **82**, 351–354 (1991).
- ¹² Roulleau, P. *et al.* Direct Measurement of the Coherence Length of Edge States in the Integer Quantum Hall Regime. *Phys. Rev. Lett.* **100**, 126802 (2008).
- ¹³ Roulleau, P. *et al.* Noise Dephasing in Edge States of the Integer Quantum Hall Regime. *Phys. Rev. Lett.* **101**, 186803 (2008).
- ¹⁴ Averin, D. V., Korotkov, A. N. & Likharev, K. K. Theory of single-electron charging of quantum wells and dots. *Phys. Rev. B* **44**, 6199–6211 (1991).
- ¹⁵ Kouwenhoven, L. P. *et al.* Electron transport in quantum dots. In *Mesoscopic Electron Transport Series E: Applied Sciences* (eds. Sohn, L. L., Kouwenhoven, L. P. & Schön, G.), vol. 345, 105–214 (Kluwer Academic, 1997).
- ¹⁶ Bonet, E., Mandar, M. D. & Ralph, D. C. Solving rate equations for electron tunneling via discrete quantum states. *Phys. Rev. B* **65**, 045317 (2002).
- ¹⁷ le Sueur, H. *et al.* Unveiling the quantum Hall regime low energy physics with energy exchange measurements (2009). Article in preparation.